Supplementary Material

A long-range planar polymer with efficient π-electron delocalization for superior proton storage

Renyuan Wang,[a1] Jing He,[a1] Minjie Shi,[a] Renwei Jing,[a] Yue Zhao,[a] Jun Yang,[a] Chao Yan,[a*] and Xingbin Yan[b*]*

[a] *School of Materials Science and Engineering, Jiangsu University of Science and Technology, Zhenjiang, 212003, P. R. China*

[b] *State Key Laboratory of Optoelectronic Materials and Technologies School of Materials Science and Engineering Sun Yat-Sen University Guangzhou 510275, P. R. China*

[*] *Corresponding author*

E-mail: shiminjie@just.edu.cn (M. Shi); chaoyan@just.edu.cn (C. Yan); yanxb3@mail.sysu.edu.cn (X. Yan)

[1] *Renyuan Wang and Jing He contributed equally to this work.*

Contents

Section 1. Materials and Methods

Materials

All of the chemical reagents, such as CH_2Cl_2, CH_3CN, $NaIO_4$, NaOAc, pyrene, and 1,2,4,5-benzenetetramine were purchased from Aladdin Chemical Reagent Co., Ltd. with analytically pure ingredients and no need for further purifications.

Characterization methods

Several characterization techniques were carried out for evaluating morphology and microstructure of the synthesized samples, including scanning electron microscope (SEM; FEI Nova NanoSem450), transmission electron microscope (TEM; Tecnai G220S-Twin), nuclear magnetic resonance spectra (NMR; Bruker Avance III spectrometer, 400 MHz), X-ray photoelectron spectroscopy (XPS; KAlpha Thermo electron), Laser Micro-Raman Spectrometer (Raman; RENISHAW inVia), and X-ray diffraction (XRD; Bruker D8 X-ray spectrometer) equipped with a 2D detector (Cu Kα, λ=1.54 Å). Thermal gravimetric analysis (TGA; TGA5500) were carried out in inert atmosphere at 10°C min^{-1} ramp up to 500 °C.

In-situ electrochemical investigations

In-situ Raman study was applied by DXR Raman microscope at the 532 nm excitation laser, wherein the laser power was set at 10 mW with a spot size of approximately 2.5 μm. The spectra were collected in transmittance mode with 4 scans at a resolution of 5 cm^{-1} within the range from 100 to 3000 cm^{-1}. In-situ Raman spectra of the PPHZ electrode were collected from in-operando monitoring mode with a series

of repetitive scans every 40 s during the GCD electrochemical testing at a current density of 1 A g^{-1}. In order to collect the in-situ UV-vis spectra during the charge and discharge process, an optical glass electrochemical tank filled with 1 M H_2SO_4 electrolyte was used as a reference cuvette (Fig. S18). The PPHZ and PHZ electrodes were put into the working cuvette for in-situ electrochemical UV-vis measurements. These reformed electrodes were discharged and charged at a current density of 1 A g^{-1}, and the UV-vis spectra were collected every 5 cycles.

Theoretical calculations

All calculations were performed by using the DFT method implemented in the commercial Gaussian 16 program package[S1]. The structures of the studied organic material as well as its complexes with protons were fully optimized at the B3LYP-D3/6-311G(d) level of theory. The solvent (H_2O) effect was included in the calculations based on polarizable continuum model (PCM) through integral equation formalism variant (IEFPCM). The vibrational frequencies of the optimized structures were carried out at the same level. Molecular surface electrostatic potential (ESP), localized orbital locator-π (LOL-π), reduced density gradient (RDG) and iso-chemical shielding surface (ICSS) wave function cubes were achieved according to the Multiwfn 3.8 (dev) code[S2] and they are visually demonstrated by using the VMD software[S3]. All of the optimized geometries mentioned were effectively constructed based on the Gaussview 6.0 approach[S4].

Electrochemical measurements

The electrode materials were prepared by mixing 70 wt% active materials, 20 wt% of acetylene black and 10 wt% PVDF binders together with the aid of NMP solution, and the uniformly mixed slurry was pressed onto the graphite paper and dried under vacuum for 8 h at 80 °C. Based on a three-electrode testing configuration, the electrochemical properties of as-prepared electrode materials were evaluated in 1 M H_2SO_4 electrolyte. Cyclic voltammetry (CV) and galvanostatic charge/discharge (GCD) measurements were conducted under different scanning rates and current densities. Electrochemical impedance spectroscopy (EIS) and Bode plots were carried out at frequencies from 100 kHz to 0.01 Hz. Long cycle testing of the electrode materials were performed using a battery testing system (LAND CT2001A) at room temperature.

Full-cell assembly

For the fabrication of a soft-package APB cell, the PPHZ polymer was applied as the anode material, while the PIND polymer was prepared (see more detail in Fig. S22) and utilized as the cathode material. The PPHZ anode, cellulose acetate separator, and the PIND cathode were packed in a sandwich arrangement (anode-separator-cathode) and encapsulated in the aluminum plastic film for packaging. After injecting 1M H_2SO_4 aqueous electrolyte, the soft-package APB cell was vacuum sealed with a sealing apparatus. For full-cell testing, two-electrode measured configuration was used to perform on evaluating the device performance. Besides, the soft-package APB cell was placed in a low-temperature coolant circulation pump (DASB-5/20) connected to a battery testing system for measuring at different temperatures.

Section 2. Synthetic Procedures

Preparation of pyrene-4,5,9,10-tetraone (monomer A)

A solution containing CH_2Cl_2 (40.0 mL) and MeCN (40.0 mL), pyrene (10 mmol), $NaIO_4$ (17.50 g, 81.8 mmol) and $RuCl_3$-xH_2O (0.25 g, 1.2 mmol) were added into deionized water (50.0 mL). The dark brown suspension was then heated at 35 °C overnight. After that, the reaction mixture was poured into 200 mL of deionized water, and the solid was removed by filtration. After the dark green product was washed with 500 mL of deionized water, the organic phase was separated. The aqueous phase was extracted with CH_2Cl_2 solution. The CH_2Cl_2 extracts were combined with the organic phase and washed with deionized water to form a dark green solution. The solvent was removed under reduced pressure to give a dark green solid, which was dried under vacuum to finally obtain pyrene-4,5,9,10-tetraone (monomer A).

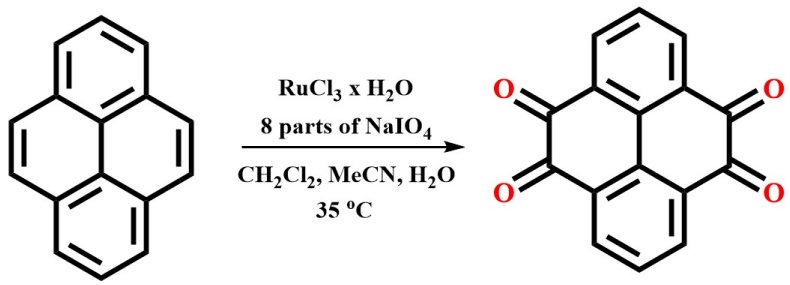

(Scheme 1)

Supplementary Figure 1. Synthesis route of the pyrene-4,5,9,10-tetraone (monomer A).

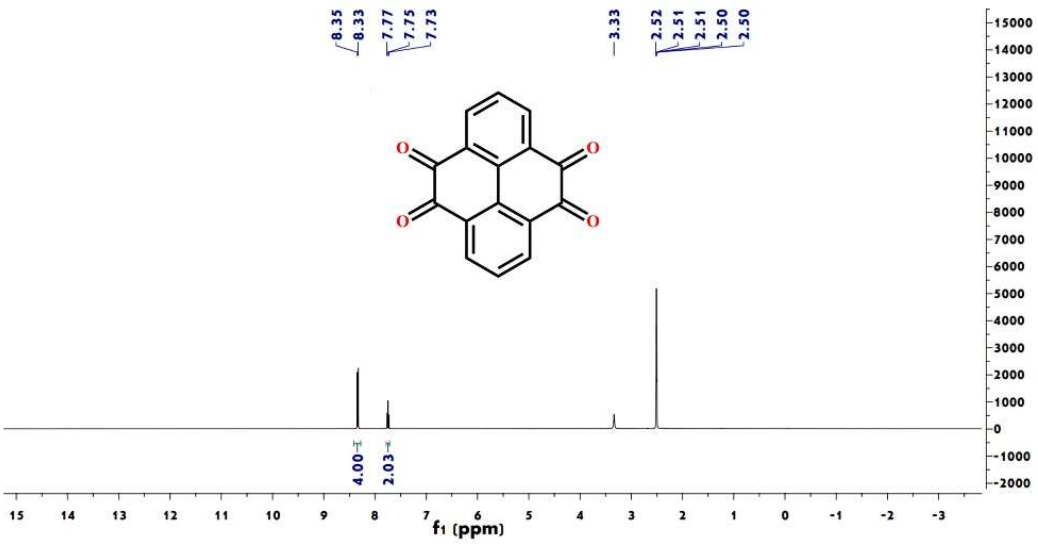

Supplementary Figure 2. ^{1}H NMR spectrum of the pyrene-4,5,9,10-tetraone (monomer A).

Preparation of phenazine-2,3,7,8-tetrayltetraamine (monomer B)

Firstly, 1,2,4,5-phenylenetetramine and NaOAc with a molar ratio of 1:1 were added into deionized water (25 mL), which were subsequently reacted at 100 ° C for 10 h under an argon atmosphere. After filtration and several times of deionized water washing, the precipitate was further purified with methanol through the Soxhlet extractor overnight. Lastly, vacuum drying at 60 ℃ resulted in phenazine-2,3,7,8-tetrayltetraamine (monomer B).

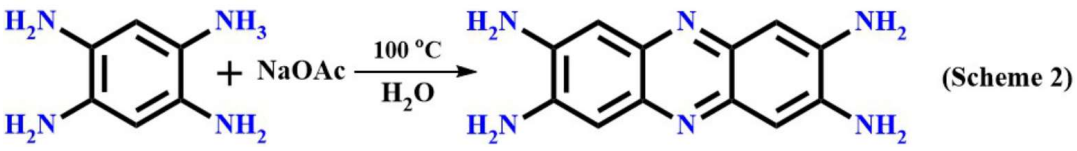

(Scheme 2)

Supplementary Figure 3. Synthesis route of the phenazine-2,3,7,8-tetrayltetraamine (monomer B).

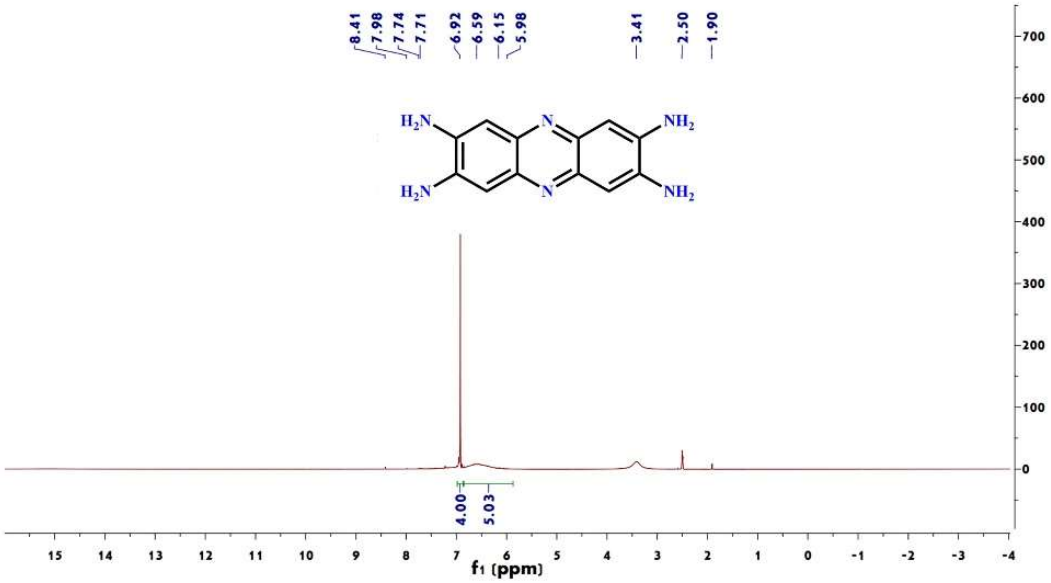

Supplementary Figure 4. ^{1}H NMR spectrum of the phenazine-2,3,7,8 tetrayltetraamine (monomer B).

Preparation of PPHZ polymer

Typically, monomer A and monomer B which the mole ratio is controlled at 1:1 were added into a 50 mL two-necked flask with acetic acid (25 mL). The above mixture was reacted at 120 °C under an argon atmosphere for 10 h. After cooling down to room temperature, the precipitate was collected by filtration and washed with acetic acid and ethanol several times, which was further purified by a Soxhlet extractor in methanol overnight. Finally, the PPHZ polymer can be successfully achieved under vacuum drying at 60 °C.

Section 3. Characterizations and Electrochemical measurements

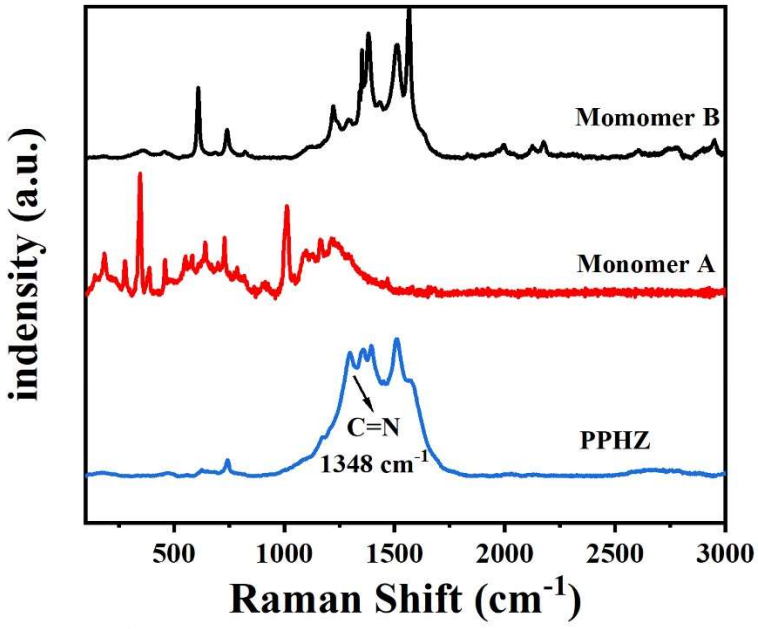

Supplementary Figure 5. Raman spectrum of monomer A, monomer B and PPHZ polymer.

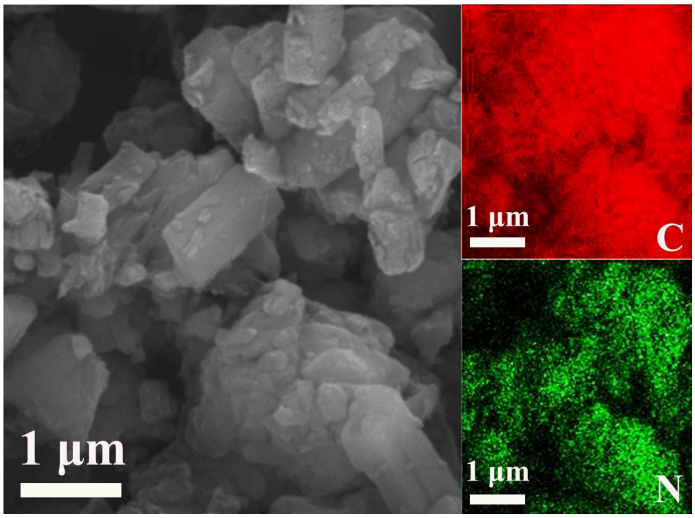

Supplementary Figure 6. SEM image and the corresponding elemental distribution mapping of the PPHZ polymer.

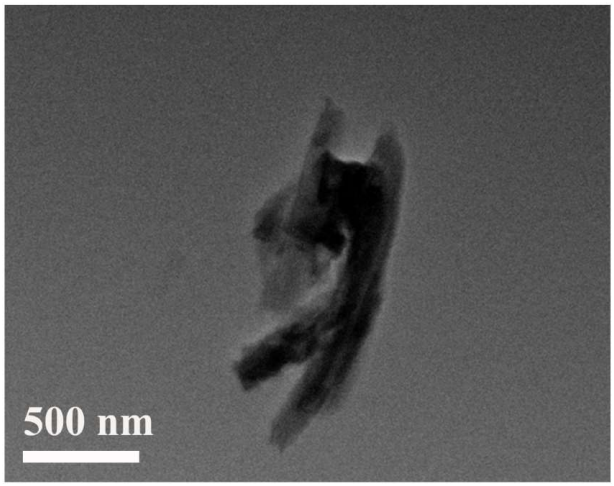

Supplementary Figure 7. TEM image of the PPHZ polymer.

The microcosmic appearance of the PPHZ polymer was revealed by SEM and TEM observations. The PPHZ polymer possesses a rod-like morphology with a length of ~ 1 μm, while the homogenous distributions of C and N species are throughout the whole polymer according to the elemental distribution mapping.

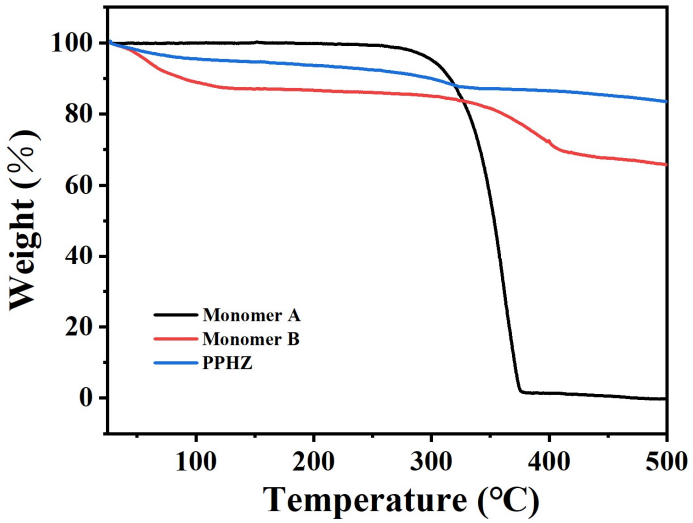

Supplementary Figure 8. TGA characterizations of monomer A, monomer B and PPHZ polymer.

The PPHZ polymer maintains a high weight retention of approximately 83.2% at 500 °C, significantly superior to its two precursors (monomer A and monomer B),

which is attributed to the extended conjugated structure with rigid framework skeleton of the PPHZ polymer.

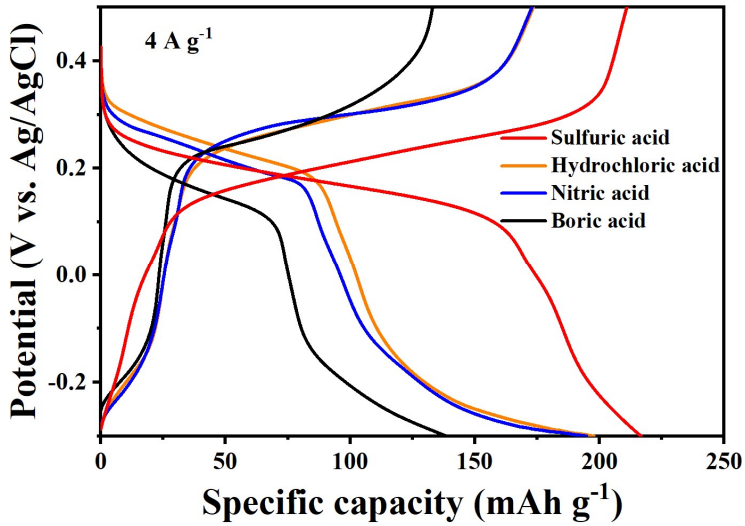

Supplementary Figure 9. GCD curves of the PPHZ electrode in different aqueous acidic electrolytes. Obviously, the redox properties can be observed from various GCD curves, showing the proton-storage capabilities of the PPHZ electrode in aqueous acidic electrolytes.

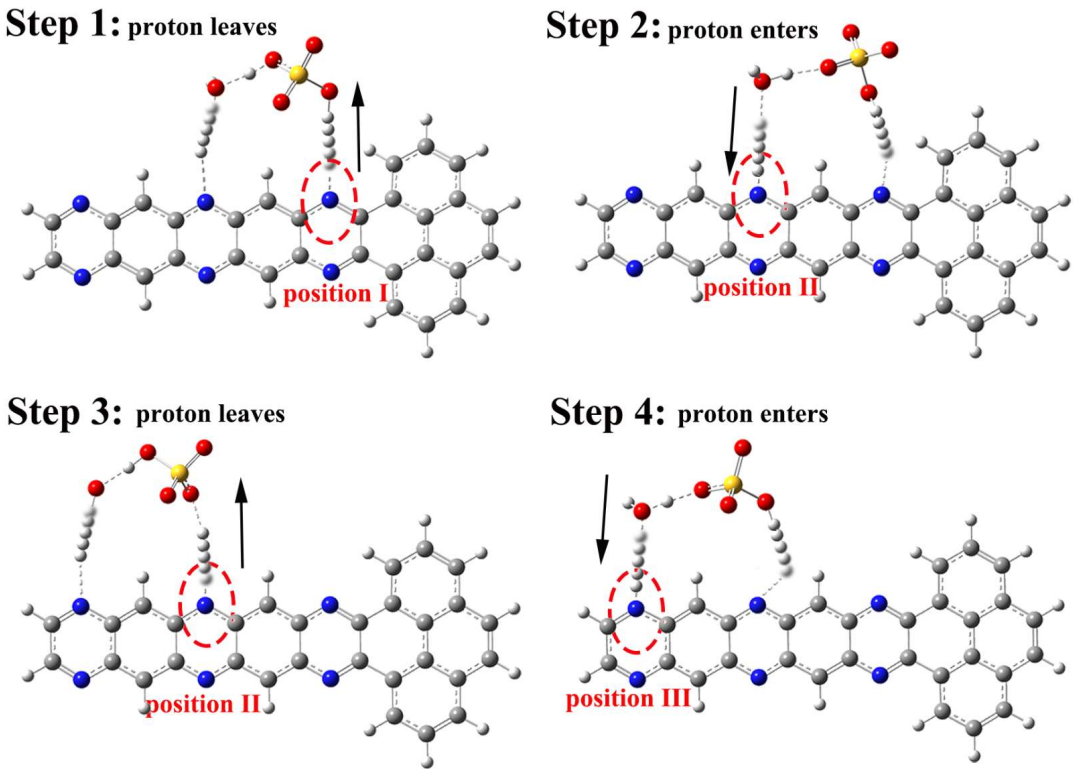

Supplementary Figure 10. Demonstration of proton diffusion through imine moieties in the PPHZ molecule.

The initial geometries of PPHZ molecule optimized under the framework of density of functional theory with B3LYP functional and 6-311G(d,p) basis set. In order to describe the dispersion interaction, the DFT-D3 dispersion correction method was also used and the transition state of proton diffusion along the polymer chain was searched by flexible potential energy surface scanning. Meanwhile, the intrinsic reaction coordinate (IRC) calculation was then performed to investigate the dynamic process of proton diffusion more intuitively. Due to the proton transport through the "Grotthus mechanism" similar to the Newtonian cradle, the hydrogen bonding network effect of solvent molecules was taken into account when calculating the proton diffusion energy barrier of PPHZ molecules. For example, proton diffusion between adjacent imine

groups through the solvent hydrogen bonding network were calculated following the diffusion paths from step 1 to step 4. With the help of solvent molecules, the proton diffuses and leaves from the vicinity of first imine group (position I) in step 1, while the hydrogen bonding network coordinate the diffusion of proton and cause proton to enter the second imine group (position II) in step 2, wherein the corresponding energy barriers of proton diffusion can be obtained during the process. Following the same way, the proton diffuses and leaves from the second imine group (position II) to the third imine group (position III) in step 3 and step 4.

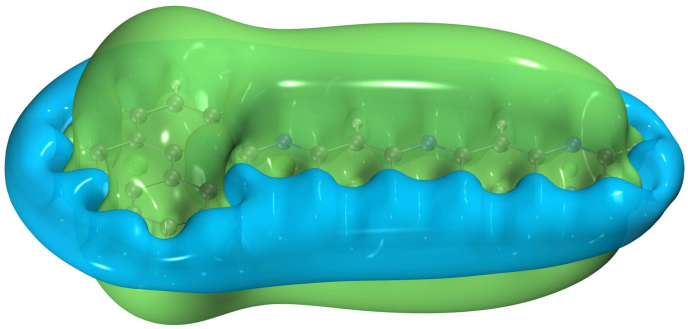

Supplementary Figure 11. Isosurface of $ICSS_{ZZ}$ in the slice plane perpendicular to the PPHZ molecule.

The B3LYP functional was adopted for the calculations based on Gaussian 16 software. For geometry optimization calculations, the def2-SVP basis set was applied. The ICSS calculation was performed with a TZVP basis set, which is a larger basis set. The DFT-D3 dispersion correction with BJ-damping was utilized to correct the weak interaction to improve the calculation accuracy. ICSS (iso-chemical shielding surfaces) analysis was performed by the Multiwfn software, wherein the visualization of the

ICSS_ZZ was achieved based on VMD software. Obviously, there are significant shielding regions protrudes in the direction perpendicular to the ring plane of the PPHZ molecule and a closed deshielding circular isosurface surrounded it. The feature of $ICSS_{ZZ}$ distribution consolidates the significant overall aromaticity of the PPHZ molecule.

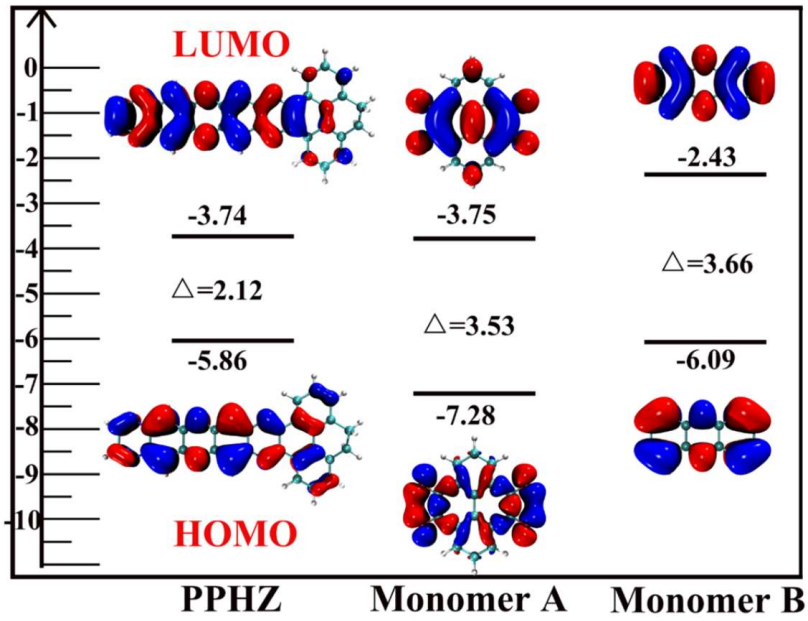

Supplementary Figure 12. Frontier molecular orbital energies of the PPHZ polymer and two types of monomers.

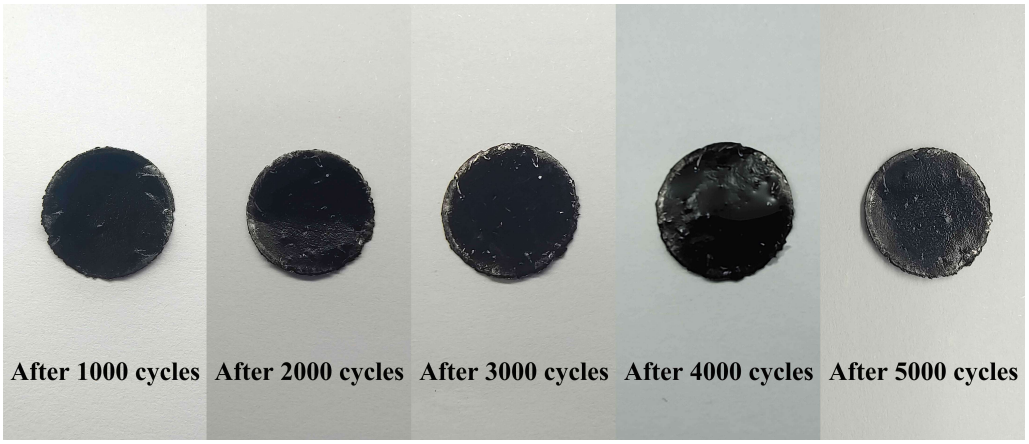

Supplementary Figure 13. Digital photos of the PPHZ electrode taken per 1000 cycles. The electrode remains intact after different charging-discharging cycles.

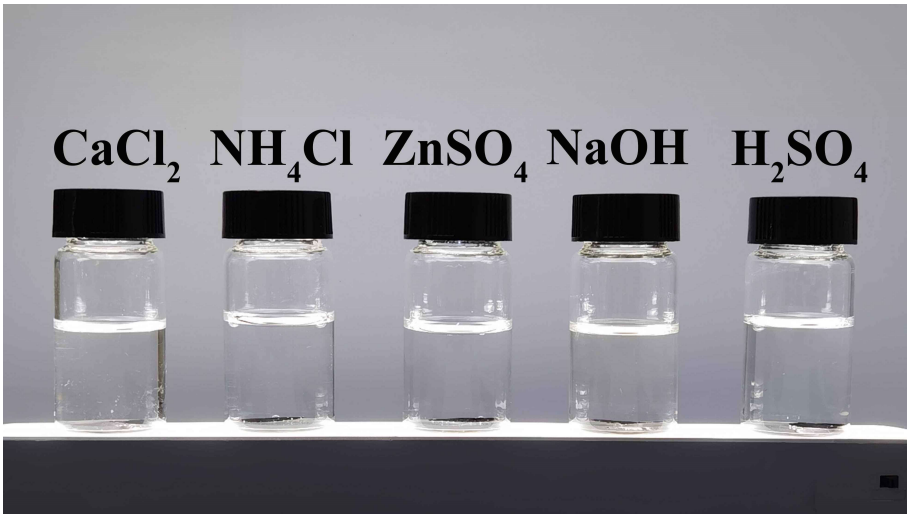

Supplementary Figure 14. Digital photos of the PPHZ electrodes soaked in different aqueous electrolytes without any dissolution after 30 days.

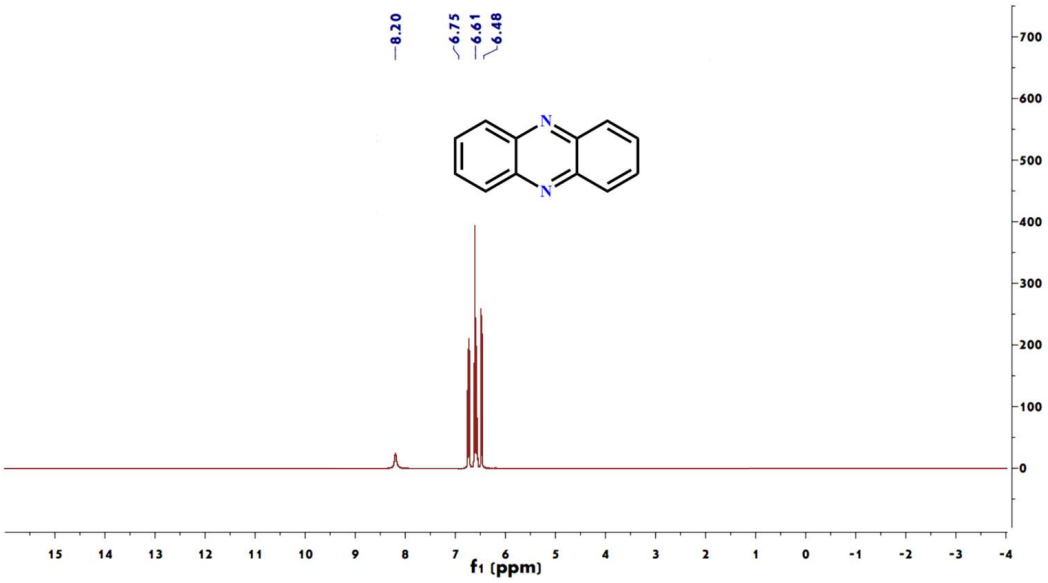

Supplementary Figure 15. ^{1}H NMR spectrum of the PHZ organic compound (small molecule compound).

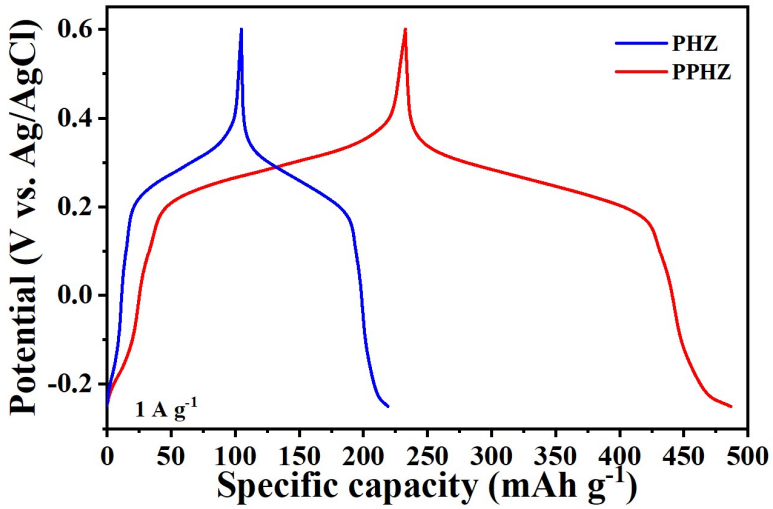

Supplementary Figure 16. Comparative GCD profiles of the PPHZ and PHZ electrodes in aqueous acidic electrolyte.

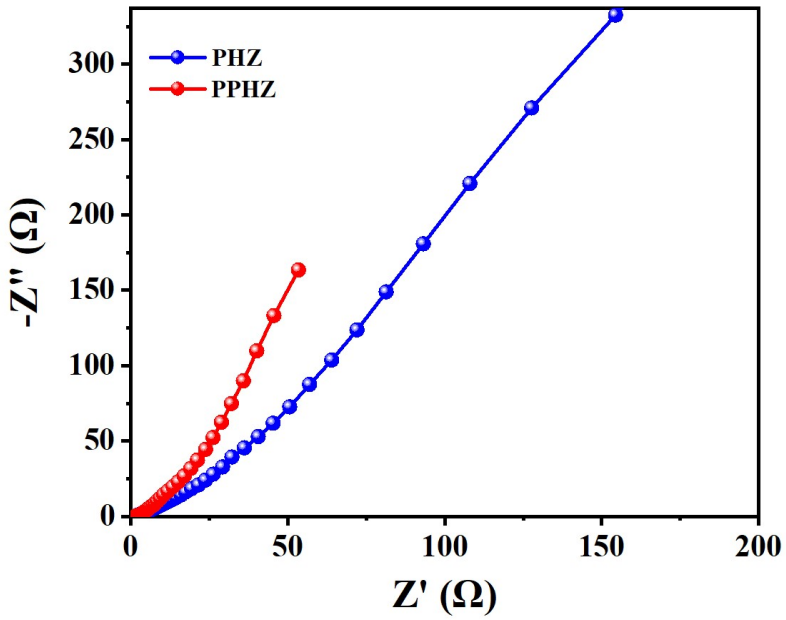

Supplementary Figure 17. EIS plots of PPHZ and PHZ electrodes in aqueous acidic electrolyte.

Compared with the PHZ electrode with small-molecular structure, the PPHZ electrode shows higher proton-storage capacity and greater electrochemical kinetic characteristics, which is owing to the superior redox activity and electron affinity of the PPHZ electrode with long-range planar and π-electron delocalized imine-rich polymeric skeleton for proton storage.

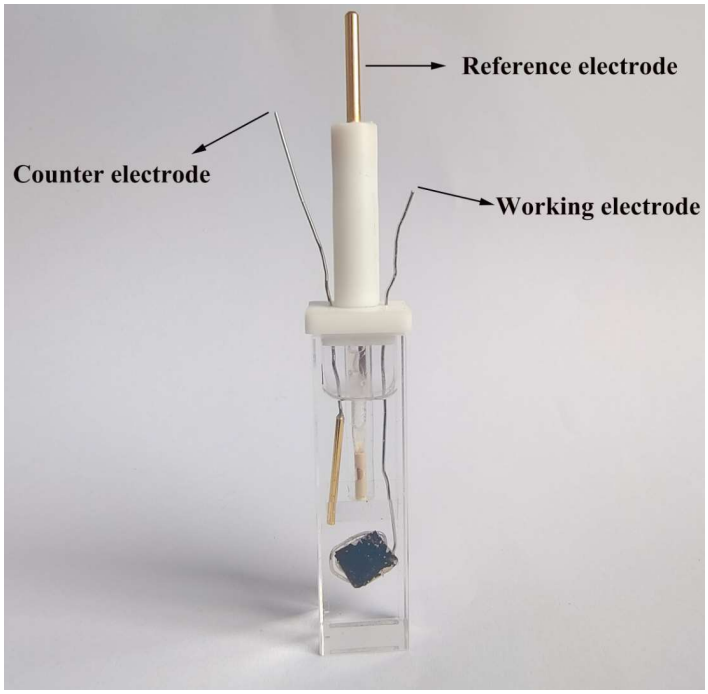

Supplementary Figure 18. Digital photo of in-situ UV-vis electrochemical cell.

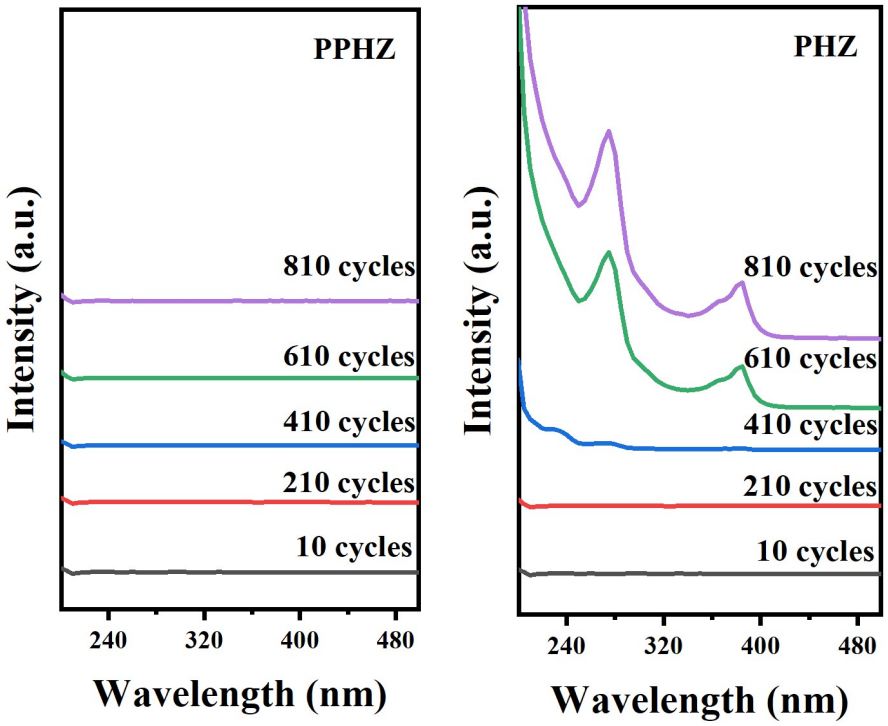

Supplementary Figure 19. Selected in-situ UV-vis spectra of aqueous acidic electrolytes within the PPHZ and PHZ electrodes after every 200 cycles.

The aqueous electrolyte within the PHZ electrode gradually shows two visible UV-

vis absorbance peaks related to the C=N group at 270 and 380 nm, indicating the obvious dissolution of the PHZ electrode after repeated cycles. By contrast, the aqueous electrolyte within the PPHZ electrode presents almost no UV-vis absorbance peak. This is because the PPHZ electrode possesses an extended polymeric backbone with strong intermolecular interactions, which contribute to its high structural stability and remarkable insolubility in aqueous electrolyte.

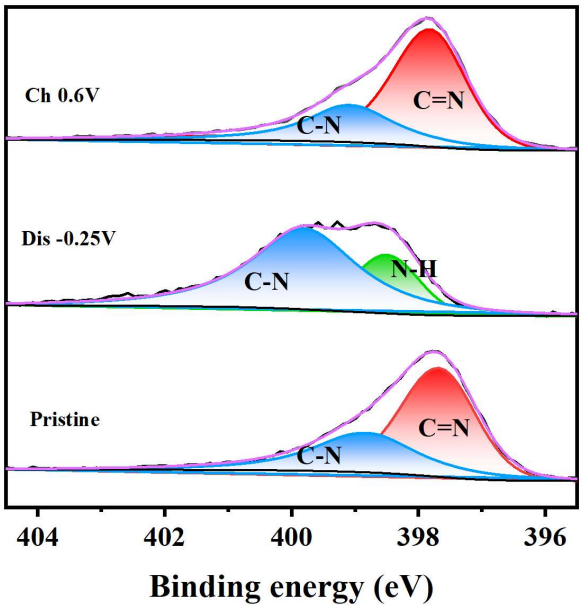

Supplementary Figure 20. XPS spectra of N 1s in the PPHZ electrode at different states.

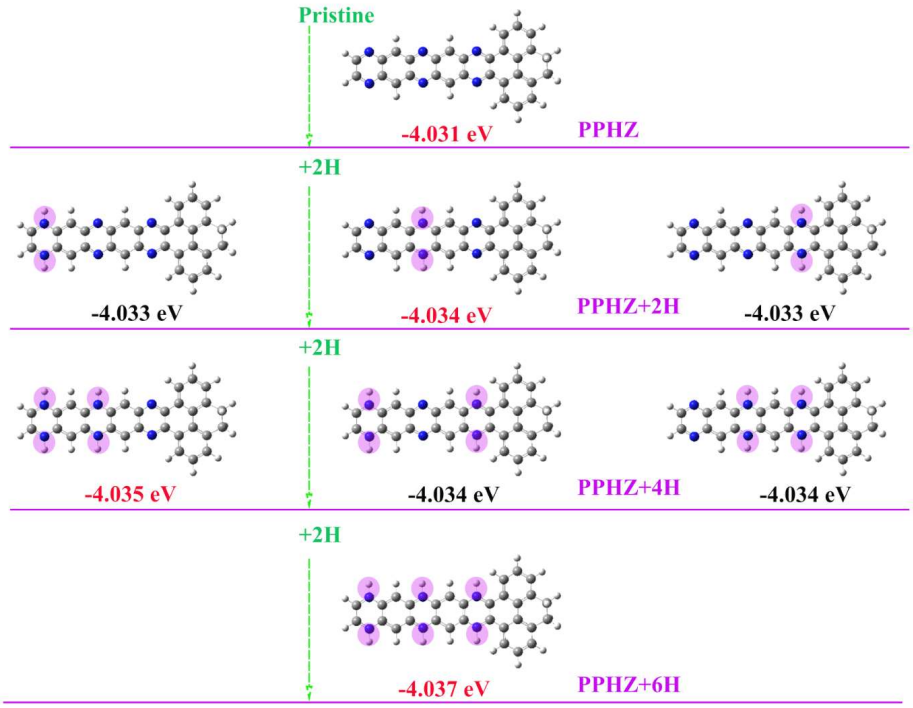

Supplementary Figure 21. Energy levels of PPHZ+xH (x represent the numbers of protons stored in PPHZ) with possible geometrical configurations during the protonated process.

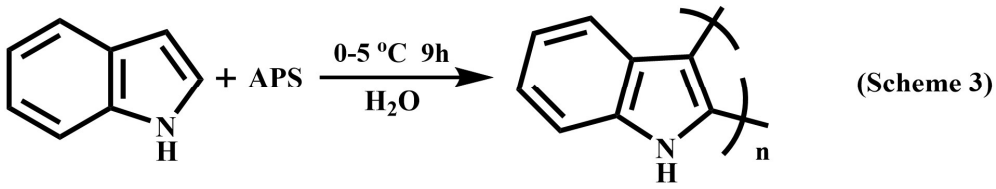

(Scheme 3)

Supplementary Figure 22. The synthesis route of PIND polymer.

Indole monomer was first dissolved in a medium of deionized water. Then the oxidant ammonium persulphate (APS) was added dropwise to the indole solution and the mixture was stirred at 0-5°C for 9 h. At the end of the reaction, the resulting PIND polymer was filtered and washed several times before vacuum drying to obtain a black powder product.

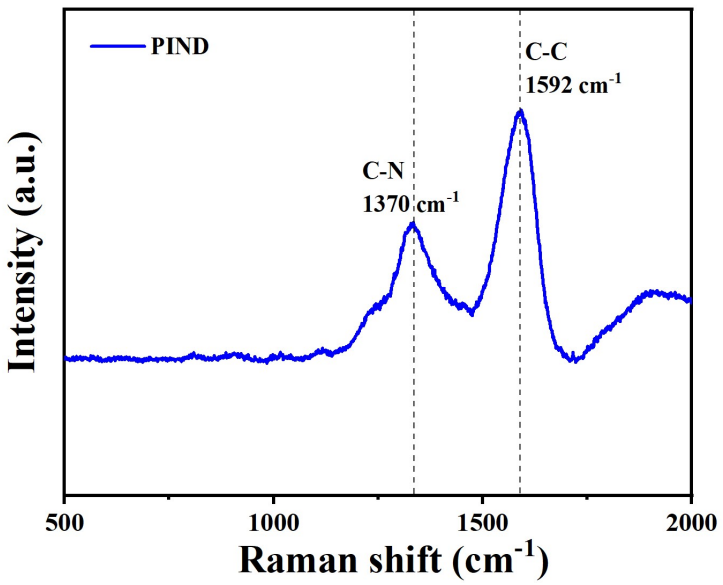

Supplementary Figure 23. Raman spectra of the PIND polymer.

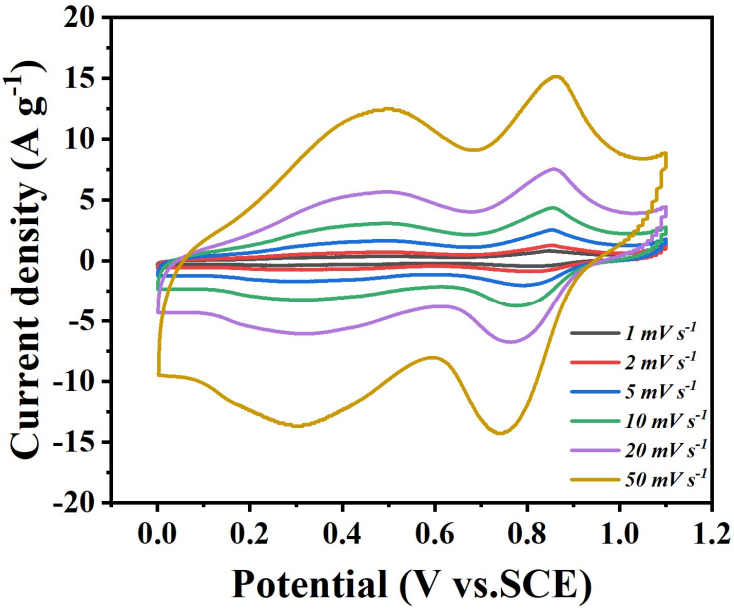

Supplementary Figure 24. CV curves of the PIND electrode in aqueous acidic electrolyte.

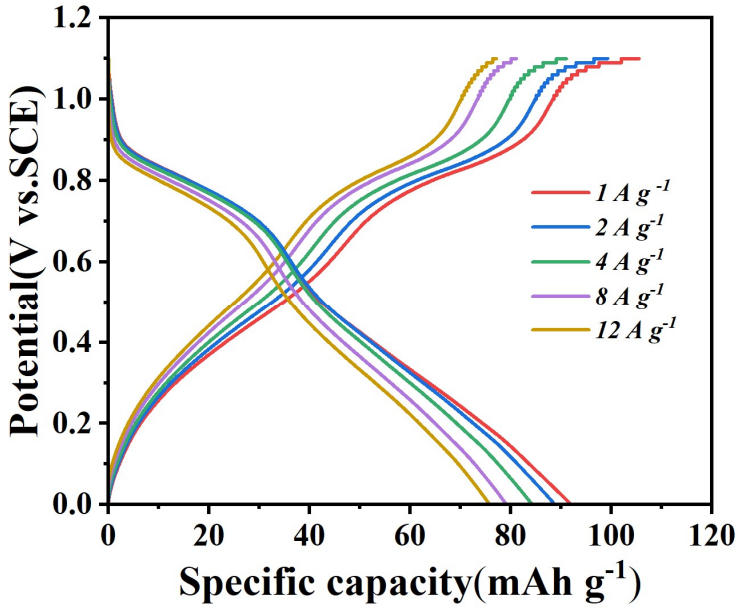

Supplementary Figure 25. GCD curves of the PIND electrode in aqueous acidic electrolyte.

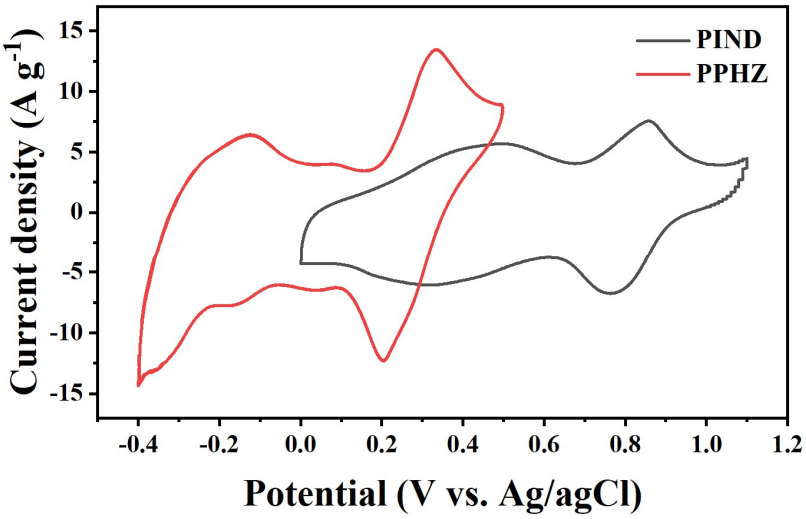

Supplementary Figure 26. Comparative CV curves of the PPHZ and PIND electrodes at 10 mV s^{-1} in aqueous acidic electrolyte within different potential ranges.

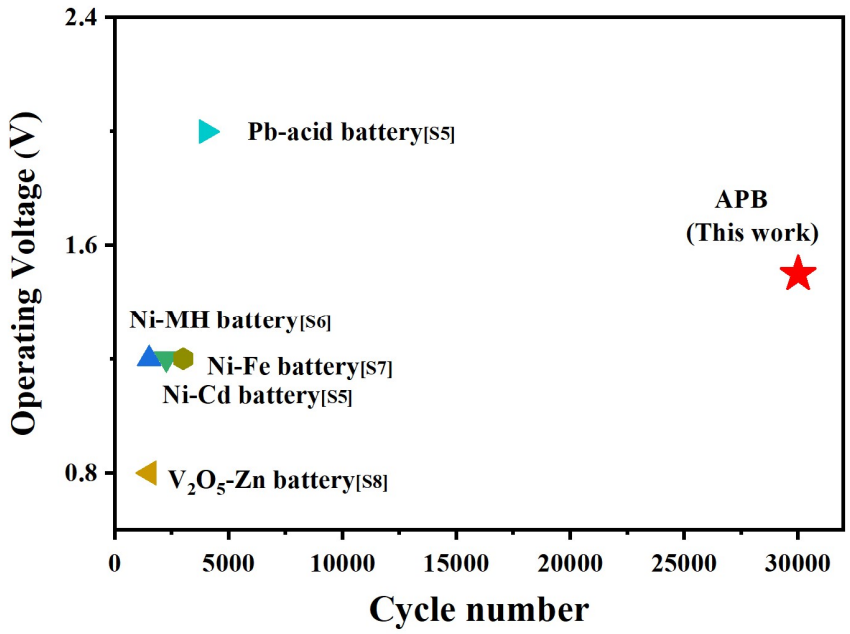

Supplementary Figure 27. Comparisons of our proposed soft-package APB with other aqueous-based batteries[S5-S8] in cycle performance and operating voltage.

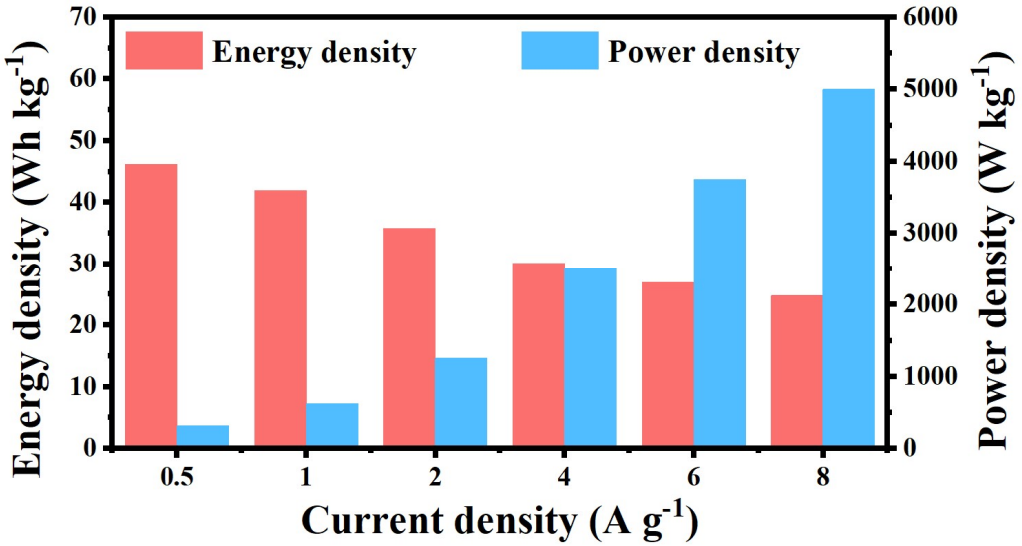

Supplementary Figure 28. Energy and power densities of the soft-package APB at different current densities.

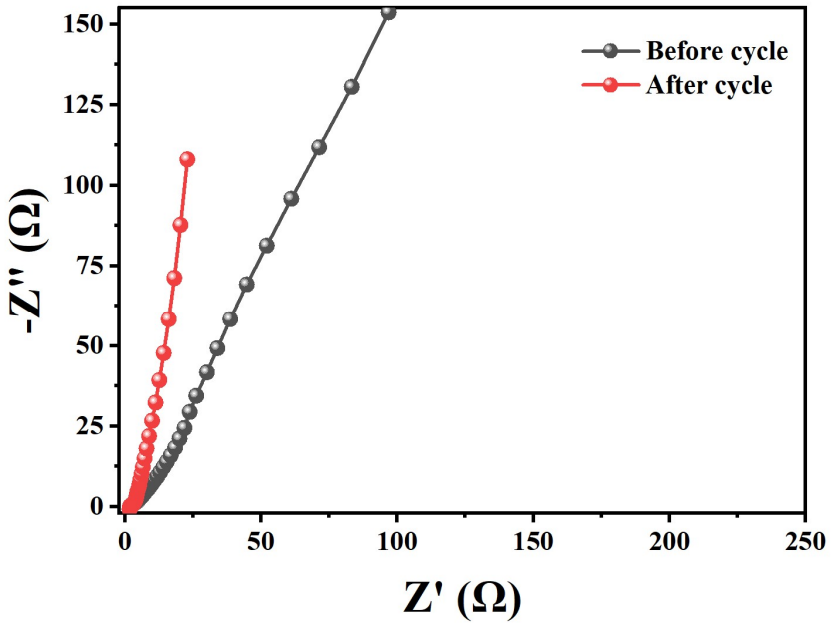

Supplementary Figure 29. Electrochemical kinetics of the soft-package APB.

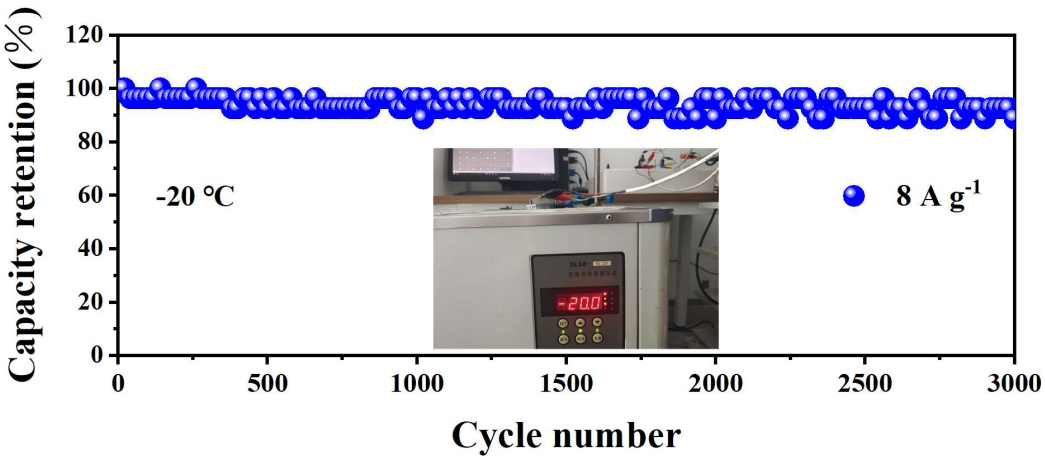

Supplementary Figure 30. Cycling performance of the soft-package APB under a low ambient temperature (-20 ℃).

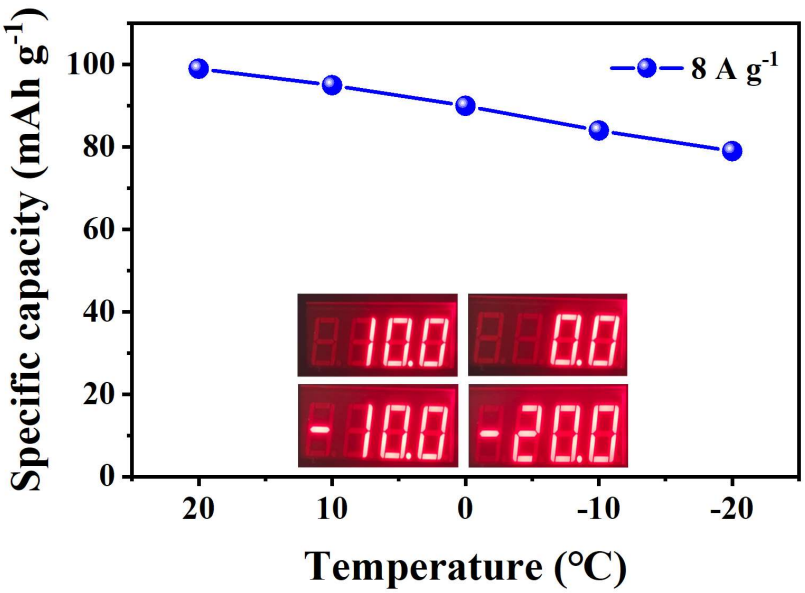

Supplementary Figure 31. Device capacities of the soft-package APB within different temperatures (20 ℃, 10 ℃, 0 ℃, -10 ℃ and -20 ℃).

Table 1. Electrochemical comparisons of our proposed APB with the existing state-of-the-art APBs based on various cathode and anode materials.

Anode material	Cathode material	Electrolyte	Voltage (V)	Life (capacity retention)	Operation temperature	Ref.
DPPZ	InHCF	0.05 M H_2SO_4	1.5 V	76.1% after 3000 cycles	25 ℃	Chem. Commun. [S9]
PNAQ	PNAQ	4 M H_2SO_4	1.1 V	70.0% after 500 cycles	25 ℃	Small Methods [S10]
PI	PR	2 M H_2SO_4 2 M $MnSO_4$	1.0 V	94.0% after 500 cycles	25 ℃	Electrochim. Acta [S11]
PI	MnO2@GF	2 M H_2SO_4 2 M $MnSO_4$	1.2 V	68.0% after 5000 cycles	25 ℃	Trends Chem. [S12]
PUQ	PTC	0.5 M H_2SO_4	1.2 V	80.0% after 1000 cycles	25 ℃	Adv. Sci. [S13]
pDTP-NQ	pDTP–AQH_2	1 M H_2SO_4	0.9 V	56.0% after 2000 cycles	25 ℃	Energy Storage Mater. [S14]
pEP(QH_2)	pEP(NQ)E	0.5 M H_2SO_4	0.5 V	50.0% after	25 ℃	Angew. Chem. Int.

E				500 cycles		Ed. [S15]
NVO	NVO	0.001 M H_2SO_4	1.6 V	65.6% after 1000 cycles	25 ℃	Electrochim. Acta [S16]
KVO	KVO	0.01 M H_2SO_4	0.8 V	84.0% after 20,000 cycles	25 ℃	Sci. China Mater. [S17]
PAS	AN-PA	2 M HCl	1.1 V	86.0% after 1000 cycles	25 ℃	J. Colloid Interface Sci. [S18]
Alizarin	Alizarin	1 M H_2SO_4	1.1 V	47.0% after 100 cycles	25 ℃	ACS Appl. Energy Mater. [S19]
PTO	MnO_2	2 M H_2SO_4 2 M $MnSO_4$	1.0 V	80.0% after 5000 cycles	25 ℃	Nat. Commun. [S20]
6AQ-4ZTC	6TCHQ-4ZTC	0.5 M H_2SO_4	1.4 V	71.0% after 500 cycles	25 ℃	Carbon [S21]
AQDS-CC	Tiron-CC	1 M H_2SO_4	0.9 V	70.0% after 600 cycles	25 ℃	ACS Appl. Mater. Interfaces [S22]
MoO_3	MnO_2@GF	2 M H_2SO_4 2 M $MnSO_4$	0.8 V	81.0% after 3000 cycles	25 ℃	ACS Energy Lett. [S23]
PPHZ	**PIND**	1 M H_2SO_4	**1.5 V**	**87.2% after 30,000 cycles** **88% after 3000 cycles**	25 ℃ -20 ℃	**This work**

Section 4. Supporting References

[S1] Frisch, M. et al. Gaussian 16, Revision A. 03, Gaussian. Inc, Wallingford CT 3, (2016).

[S2] Lu, T., Chen, F. Multiwfn: a multifunctional wavefunction analyzer. *J. Comput. Chem.* **33**, 580-592 (2012).

[S3] Humphrey, W., Dalke, A. & Schulten, K. VMD: visual molecular dynamics. *J. Mol. Graph.* **14**, 33-38 (1996).

[S4] Inc, Semichem. GaussView 6.0.16 program: http://gaussian.com/gaussview6/ (accessed on Nov 25, 2019).

[S5] Argyrou, MC., Christodoulides, P. & Kalogirou, SA. Energy storage for electricity generation and related processes: technologies appraisal and grid scale applications. *Renew. Sust. Energ. Rev.* **94**, 804-821 (2018).

[S6] Schmidt, O., Hawkes, A. & Gambhir, A. Staffell I. the future cost of electrical energy storage based on experience rates. *Nat. Energy* **2**, 1-8 (2017).

[S7] Reddy, T.B. Linden's handbook of batteries. McGraw-Hill Education (2011).

[S8] Kundu, D., Adams, B.D., Duffort, V., Vajargah, S.H. & Nazar, L.F. A high-capacity and long-life aqueous rechargeable zinc battery using a metal oxide intercalation cathode. *Nat. Energy* **1**, 16119 (2016).

[S9] Qiao, J. et al. A rechargeable aqueous proton battery based on a dipyridophenazine anode and an indium hexacyanoferrate cathode. *Chem. Commun.* **57**, 4307-4310 (2021).

[S10] Sun, T. et al. Bipolar organic polymer for high performance symmetric aqueous proton battery. *Small Methods* **5**, 2100367 (2021).

[S11] Han, W., Li, M., Ma, Y. & Yang, J. Dianhydride-based polyimide as organic electrode materials for aqueous hydronium-ion battery. *Electrochim. Acta* **403**, 139550 (2022).

[S12] Wu, Z., Yang, P., Wang, S., Li, S. & Zhang, S. Emerging organic electrode materials for aqueous proton batteries. *Trends Chem.* **4**, 1121-1134 (2022).

[S13] Zhu, M. et al. Bioinspired catechol-grafting pedot cathode for an all-polymer aqueous proton battery with high voltage and outstanding rate capacity. *Adv. Sci.* **9**, 2103896 (2022).

[S14] Wang, X., Zhou, J. & Tang W. Poly(dithieno[3,2-b:2',3'-d]pyrrole) twisting

redox pendants enabling high current durability in all-organic proton battery. *Energy Storage Mater.* **36**, 1-9 (2021).

[S15] Strietzel, C. et al. An aqueous conducting redox-polymer-based proton battery that can withstand rapid constant-voltage charging and sub-zero temperatures. *Angew. Chem. Int. Ed.* **59**, 9631-9638 (2020).

[S16] Lv, N. et al. Ultralow-concentration electrolyte unlocking the high-stable proton storage in $(NH_4)_{0.5}V_2O_5$ electrode. *Electrochim. Acta* **431**, 141097 (2022).

[S17] Dong, S. et al. Ultralow-concentration electrolyte boosting $K_{0.486}V_2O_5$ for high-performance proton storage. *Sci. China Mater.* **65**, 3069-3076 (2022).

[S18] Lakshmi, K.S. et al. Molecularly engineered organic copolymers as high capacity cathode materials for aqueous proton battery operating at sub-zero temperatures. *J. Colloid Interface Sci.* **619**, 123-131 (2022).

[S19] Tong, L., Jing, Y., Gordon, R.G. & Aziz, M.J. Symmetric all-quinone aqueous battery. *ACS Appl. Energy Mater.* **2**, 4016-4021 (2019).

[S20] Guo, Z. et al. An organic/inorganic electrode-based hydronium-ion battery. *Nat. Commun.* **11**, 959 (2020).

[S21] Nueangnoraj, K., Tomai, T., Nishihara, H., Kyotani, T. & Honma, I. An organic proton battery employing two redox-active quinones trapped within the nanochannels of zeolite-templated carbon. *Carbon* **107**, 831-836 (2016).

[S22] Xu, Y., Zheng, Y., Wang, C. & Chen Q. An all-organic aqueous battery powered by adsorbed quinone. *ACS Appl. Mater. Interfaces* **11**, 23222-23228 (2019).

[S23] Yan, L. et al. Solid-State Proton Battery Operated at Ultralow Temperature. *ACS*

Energy Lett. **5**, 685-691 (2020).